

33rd EUROPEAN ROTORCRAFT FORUM

Session Aerodynamics
Paper #042

**ACTIVE ROTOR PERFORMANCE INVESTIGATIONS
USING CFD/CSD WEAK COUPLING**

by

M. Dietz*, E. Krämer*, S. Wagner*, A. Altmikus**

*INSTITUT FÜR AERO- & GASDYNAMIK, UNIVERSITÄT STUTTGART,
70550 Stuttgart, Germany

**EUROCOPTER DEUTSCHLAND GmbH, 81663 München, Germany

SEPTEMBER 11 - 13, 2007
KAZAN
RUSSIA

ACTIVE ROTOR PERFORMANCE INVESTIGATIONS USING CFD/CSD WEAK COUPLING

M. Dietz^{*}, E. Krämer^{*}, S. Wagner^{*} and A. Altmikus^{**}

^{*}Institut für Aerodynamik und Gasdynamik, Universität Stuttgart, Stuttgart, Germany

^{**}Eurocopter Deutschland GmbH, Munich, Germany

Key Words: Active Rotor, Fluid-Structure Coupling, Weak Coupling, Rotor Performance

Abstract. Active rotor concepts are of high interest in today's helicopter research due to their potential in noise and vibration reduction and in reduction of the required rotor power. In the frame of the research projects ADASYS and LARS Eurocopter has developed an active flap rotor whose first flight on a BK117 C2 prototype demonstrator took place in September 2005. In a close cooperation between Eurocopter Deutschland and the Institute of Aerodynamics and Gasdynamics numerical simulations of the active rotor concept have been performed. First results have been published at the ERF 2005. In the past two years the numerical modelization has been improved and further investigations have been carried out. This paper presents recent active rotor performance results for both the active flap rotor and a new concept replacing the discrete flap by an active trailing edge. The weak coupling method between the CFD solver FLOWer and the flight mechanics code HOST is applied to the isolated rotor in order to obtain a trimmed rotor solution.

Nomenclature

μ	advance ratio
Ma	Mach number
θ_0	collective pitch angle [°]
θ_C	longitudinal cyclic pitch [°]
θ_S	lateral cyclic pitch [°]
α_q	rotor shaft angle [°]
C_T	thrust coefficient
C_Q	torque coefficient
C_{Mx}	rotor mast roll moment coefficient
C_{My}	rotor mast pitch moment coefficient
$C_n Ma^2$	sectional normal force coefficient
$C_m Ma^2$	sectional pitching moment coef.
$C_{Fz} Ma^2$	sectional thrust coefficient (in z-direction of rotating system)
$C_{Fy} Ma^2$	sectional drag coefficient (in y-direction of rotating system)
$C_{Mx} Ma^2$	sectional moment coefficient (around x-direct. of rotating system)
ψ	Azimuth angle
φ	Phase angle of the HHC-law

Acronyms

CFD	Computational Fluid Dynamics
CSD	Computational Structure Dynamics
DLR	Deutsches Zentrum für Luft- und Raumfahrt e.V.
ECD	Eurocopter Deutschland GmbH
HOST	Helicopter Overall Simulation Tool
IAG	Institut für Aerodynamik und Gasdynamik
LARS	Lagerloses Aktives Rotor System
HHC	Higher Harmonic Control
TFI	Transfinite Interpolation

Coordinate Systems

Both the rotating rotor hub system and the non-rotating rotor hub system correspond to the definitions used by HOST.

Rotating rotor hub system

- x-axis in radial direction from root to tip
- y-axis in tip path plane trailing to leading edge
- z-axis in rotor hub direction

Non-rotating rotor hub system

- x-axis longitudinal pointing backwards
- y-axis lateral pointing to starboard
- z-axis in rotor hub direction

An upward flap deflection corresponds to a positive deflection angle.

Introduction

In case of a conventional rotor a certain trim state is achieved by the collective and cyclic pitch input into the blade root via the swash plate. By adapting the collective and cyclic pitch the rotor is trimmed towards a set of mean loads at the rotor center, leading to a force and moment equilibrium around the helicopter's center of gravity and thus to a steady flight condition. These mean rotor loads are uniquely defined by the flight condition to be achieved. In case of a conventional ("passive") rotor this requires a unique articulation of the swash plate which is equivalent to a unique set of control angles. This is due to the fact that the swash plate only allows for a 1/rev cyclic control input into the rotor.

Active rotor control allows for an individual high-frequency pitch control of the main rotor blades. The additional degrees of freedom introduced by active control override the unique correlation between trim state and control input. It is thus possible to achieve a certain trim state of the rotor using different control laws. The essential point about higher harmonic control is that a certain control law might be superior to other control laws or to the corresponding passive rotor with respect to vibratory rotor loads, blade vortex interaction or rotor performance.

The active rotor concept developed by Eurocopter uses either actively controlled trailing edge flaps or an active elastic trailing edge. The active flap rotor has been developed in the frame of the research project LARS and successfully flown on a BK117 C2 prototype demonstrator in September 2005^[4]. The active trailing edge concept is currently developed in the frame of the research project FRIEND-COPTER.

The objective of the present paper is to investigate both concepts with respect to power consumption in steady forward flight. In order to allow for a meaningful comparison between different flap control laws and to the passive rotor the numerical simulations need to be trimmed towards an identical flight condition. We use the a weak coupling method between the CFD method FLOWer (DLR) and the flight mechanics/CSD code HOST (Eurocopter), in order to take fluid-structure coupling effects into account and to trim the rotor towards the predefined trim objectives. The selected trim objectives (which have been previously identified from flight test data) are the rotor thrust and the longitudinal and lateral mast moments (C_T , C_{Mx} , C_{My}). The objective is met by iteratively adjusting the collective and cyclic

pitch input (θ_0 , θ_C , θ_S). The rotor shaft angle α_q has been held fixed for all investigations.

The results presented at the ERF 2005^[14] focussed on the pure aerodynamic effect of the flap deflection, as the structural properties of the active blades have not yet been taken into account. Although from an aerodynamic point of view the active blade is almost identical to the passive one, it differs significantly from a dynamic point of view. In order to facilitate a adequate control authority by the active control the active blade is torsionally much softer than the passive one.

The present paper focusses on three aspects:

- Firstly, we will present the performance results that have been obtained for the trailing edge flap rotor (LARS configuration) using the structural model of the active rotor. At the same time, the results will be compared to a generic scenario, for which the trailing edge flap has been replaced by the elastic trailing edge.
- For the optimum flap control angle, the influence of the flight speed on the rotor power requirement will be discussed.
- In the third part, we will present preliminary rotor performance results for the actual FRIENDCOPTER configuration utilizing elastic trailing edge flaps.

Numerical Methods

Structure model (HOST)

The EUROCOPTER flight mechanics tool HOST^[7] represents a computational environment for simulation and stability analysis of the complete helicopter system. It enables the study of single helicopter components like isolated rotors as well as complete configurations with related substructures.

As a general purpose flight mechanics tool, HOST is capable of trimming the rotor based on a lifting-line method with 2D airfoil tables. For the flap, an additional interpolation is done in the polar curves depending on the flap angle.

Since the active rotor of Eurocopter Deutschland is conceived as a servo-flap rotor,^{[1]-[4]} the elastic motion is also of great importance for a reliable prediction.

The elastic blade model in HOST considers the blade as a quasi one-dimensional Euler-Bernoulli beam. It allows for deflections in flap and lag direction and elastic torsion along the blade axis. In addition to the assumption of a linear material law, tension elongation and shear deformation are neglected. However,

possible offsets between the local cross-sectional centre of gravity, tension centre and shear centre are accounted for, thus coupling bending and torsional DOFs.

The blade model is based on a geometrically non-linear formulation, connecting rigid segments through virtual joints. At each joint, elastic rotations are permitted about the lag, flap and torsion axes. Since the use of these rotations as degrees of freedom would yield a rather large system of equations, the number of equations is reduced by a modal Rayleigh-Ritz approach. A limited set of mode-like deformation shapes together with their weighting factors are used to yield a deformation description. Therefore, any degree of freedom can be expressed as,

$$h(r, \psi) = \sum_{i=1}^n q_i(\psi) \cdot \hat{h}_i(r) \quad (1)$$

where n is the number of modes, q_i the generalized coordinate of mode i (a function of the azimuth angle ψ), and \hat{h}_i is the modal shape (a function of the radial position r).

Aerodynamic model (FLOWer)

In the present study FLOWer^[8] has been used for the aerodynamics, which is available at IAG and ECD through the cooperation with the DLR in the framework of the CHANCEll and SHANEL projects. FLOWer solves the three-dimensional, unsteady Euler or Reynolds-averaged Navier-Stokes equations in order to analyze the flow field around the helicopter rotor. These equations are formulated in a hub attached, non-inertial, rotating frame of reference, with explicit contributions of centrifugal and Coriolis forces. See [9] for details of the algorithm.

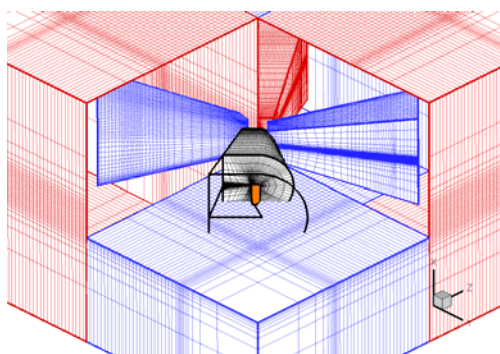


Figure 1: Chimera grid setup

The discretisation of space and time is separated by the method of lines using a cell-vertex or cell-centered finite volume formulation. Spurious oscillations of the central difference scheme are suppressed by first and second order artificial dissipation. The time

integration makes use of the dual time stepping technique with a second order implicit time integration operator.^[10]

FLOWer features the Chimera technique, allowing for arbitrary relative motion of aerodynamic bodies. Body fitted grids around each blade are embedded in a background grid (Figure 1), in which the blade vortex sheets are convected from one blade grid to the next.

Weak Coupling

The iterative coupling scheme used for the present work basically corresponds to the technique used in [11]-[13]. HOST uses CFD loads to correct its internal 2D aerodynamics and re-trims the rotor. The blade dynamic response is introduced into the CFD calculation in order to obtain updated aerodynamic loads. This cycle is repeated until the CFD loads match with the blade dynamic response evoked by them. A criterion for this converged state is given by the change in the free controls with respect to the preceding cycle. Convergence has been reached after the changes in the controls have fallen below this imposed limit. The specific steps of the coupling procedure and further details can be extracted from [14].

The weak coupling strategy was applied to the passive and active rotors in the same manner. In the case of the active rotor, HOST uses modified polar curves in the flap region for its internal 2D aerodynamics. From the CFD perspective the blade loading is directly influenced by the local grid deformation in the flap region. The resulting load distribution is taken into account by HOST for the rotor trim in the same way as for the passive rotor.

Grid Deformation

In order to correctly model the dynamic behaviour of the rotor blade in the CFD solver, the blade surface and the surrounding grid system must be deformed according to the output of the preceding HOST calculation. The specific steps required to reconstruct the blade's elastic axis and torsion distribution from the data provided by HOST are given in [14].

Our previous investigations were lacking a grid deformation tool with a multi-block capability. Hence, we were restricted to single-block blade grids, which caused problems both in the grid generation process and the achievable grid quality. In the meantime this drawback has been eliminated, as the grid deformation tool has been extended towards the treatment of multi-block topologies. A detailed description of the tool will be given in a forthcoming paper. However, a brief description of the basic deformation method is given in the following.

The deformation tool is based on the algebraic deformation method originally proposed by Hierholz^[15]. It uses Transfinite Interpolation (TFI) based on Hermite polynomials in order to reduce the prescribed deformation at the boundary (i.e. the blade surface) to zero towards the outer boundary of the grid block. In order to allow for the treatment of multi-block topologies the deformation process is splitted into two parts:

- In the first step, all blocks in a plane contact to the blade surface are deformed. The deformation process takes both a translatory and a rotatory portion into account. The rotatory portion of the TFI guarantees that the angle of the body-normal grid lines leaving the blade surface is conserved with respect to the surface normal during the deformation process. This procedure is essential in order to maintain the grid quality within the boundary layer. The grid deformation process of the blocks contributing to the blade surface results in deformed cut faces along the body-normal index planes. These deformed cut faces are used as predefined deformation for the blocks not contributing to the blade surface.
- In the second step all blocks not contributing to the blade surface are deformed, utilizing the deformed cut faces obtained in the first step as prescribed deformations. If prescribed cut faces are available along more than one index direction, the deformation process along the index directions is carried out sequentially. Only the translation part of the TFI is taken into account for these blocks.

Figure 2 illustrates the grid deformation process of the blade grid structure by means of the undeformed blade surface (gray) together with the deformed surface (blue), a section of the deformed grid (red) and the block boundaries of the deformed grid (blue).

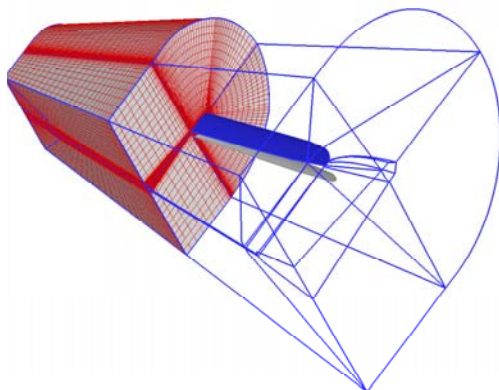


Figure 2: Blade grid deformation

Results

Phase Sweep for LARS configuration

The test case presented in this section corresponds to the one that has already been used in [14] and [16]. Compared to the results presented in [16], the grid resolution of the blade grids has almost been doubled in order to check for the grid independency of the performance results. Additionally, we will present the results obtained by replacing the discrete trailing edge flap by an elastic trailing edge with an identical trailing edge deflection. Please note, that this represents a generic scenario as the elastic trailing edge geometry does not match to the one proposed in the FRIENDCOPTER project. The elastic trailing edge results should thus be considered as a pure validation test case in order to check the correct implementation of the model.

The test case represents a forward flight case with a medium advance ratio of $\mu=0.3$. For both the passive and the active rotor the shaft angle was held fixed at $\alpha_q=-4.9^\circ$ and the calculations were trimmed for thrust, lateral and longitudinal mast moment by adaptation of the free controls $\theta_b, \theta_c, \theta_s$. Flight condition and trim objective are summarized in Table 1.

The active ATR-A rotor blade (LARS configuration) features three adjoining flap segments with a chordwise extent of 15% chord and the radial positions $r/R = 0.69 - 0.75$, $r/R = 0.75 - 0.8$ and $r/R = 0.8 - 0.85$. For the present calculations a common control law was used for the innermost and the central flap segment, whereas the outermost segment remains fixed at zero deflection. The 2/rev flap control law is given by:

$$A(t) = A_0 \cdot \cos(2 \cdot \Omega \cdot t - 2 \cdot \varphi) \quad (2)$$

For the discrete (rigid) trailing edge flap model the flap amplitude was prescribed to $A_0=6^\circ$. In case of the elastic trailing edge model the flap geometry has been left unmodified and the trailing edge deflection has been set equivalent to the 6° deflection of the rigid flap. Figure 3 compares both chordwise deflection shapes. It can easily be seen that the identical amplitude at the trailing edge leads to a stronger deflection of the flow in case of the elastic trailing edge. Hence, an increased control authority of the elastic trailing edge, combined with an increased drag in the flap region, can be expected.

Table 1: Flight condition and trim objective

Flight speed Mach number	0.21
Blade tip Mach number	0.64
Blade tip Reynolds number	4.7×10^6
Rotor shaft angle	-4.9 deg
Far field pressure	84400 Pa
Far field temperature	279 K
Thrust coefficient	0.008
Rotor mast pitch moment cf.	-0.636×10^{-4}
Rotor mast roll moment coef.	-0.193×10^{-4}

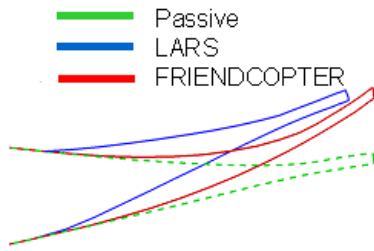


Figure 3: Comparison of flap geometries

The CFD computations have been carried out using the Chimera grid system depicted in Figure 1. The blade grids have been obtained from a refinement of the grids used in [14]. Hence, for this investigation we haven't yet made use of the multi-block capability of the grid deformation tool. The grid resolutions are given in Table 2.

Table 2: Grid resolution

Grid	Resolution	Number of cells
Blade grid	185x37x133	874,368
Background grid	4 x 65x73x73	1,327,104

Note, that in contrast to the computations presented in [14], we switched from the Baldwin-Lomax turbulence model to the two-equation $k\omega$ -Wilcox model in order to improve the prediction of the flow separation on the retreating blade side. An azimuthal resolution of 1° per time step was used for all computations presented in this paper.

Trim convergence

The convergence in the control angles θ_0 , θ_C and θ_S versus the trim iterations is given in Figure 4. The Figure shows the convergence for the passive rotor and the active rotor with trailing edge flap. Due to the limited space the convergence of the active rotor with elastic trailing edge is not shown. However, convergence properties are comparable to the ones of the trailing edge flap rotor. The Figure

shows that a converged solution is obtained after four re-trims. Although the blade is torsionally much softer than the one used in [14], convergence properties are still very good. After four re-trims the changes in all control angles have fallen below 0.01° .

In Figure 5 the unsteady aerodynamic rotor loads are shown for the complete weak coupling process, exemplarily for the passive rotor. Each re-trim is marked off with respect to the preceding trim by the line type change from solid to dash. It can be clearly seen that the disturbance introduced by the update of the blade dynamic response decreases from each retrim cycle to the next as the procedure converges towards the trimmed state.

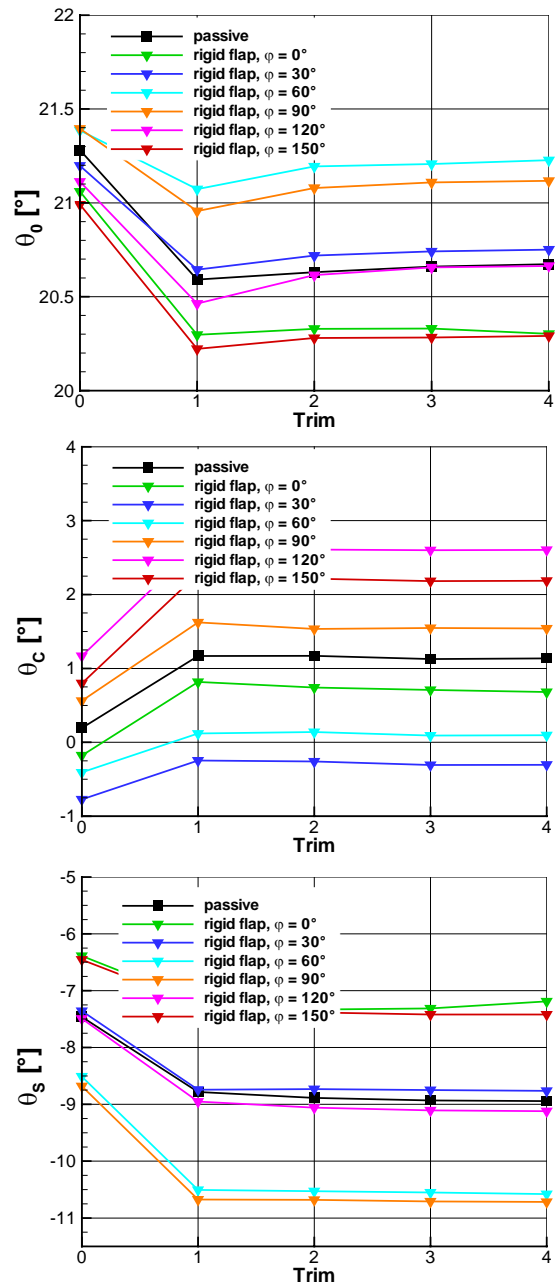


Figure 4: Convergence of collective and cyclic pitch angles

Figure 6 proves that the prescribed trim objective has actually been reached. The Figure shows the mean value of the unsteady rotor thrust, rotor roll moment and rotor pitch moment for the last quarter revolution of each trim cycle. The Figure includes the variation of the mean values for the passive rotor and the two types of active flaps at a phase angle of $\varphi = 150^\circ$. One can see, that all loads – although starting at different levels for the 0th trim – converge towards identical values during four re-trim cycles. A trimmed state as given after trim 4 is the prerequisite in order to allow for a meaningful comparison between the passive and the active rotor.

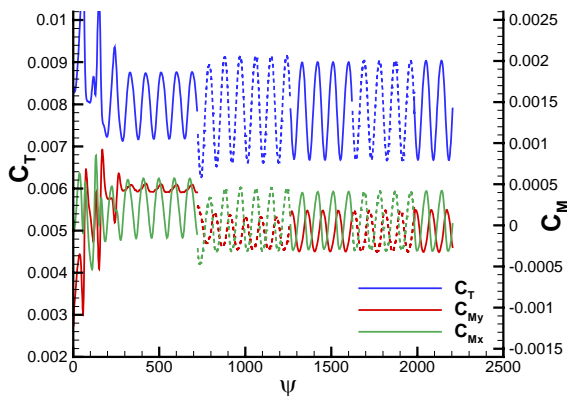


Figure 5: Unsteady rotor load coefficients (passive rotor)

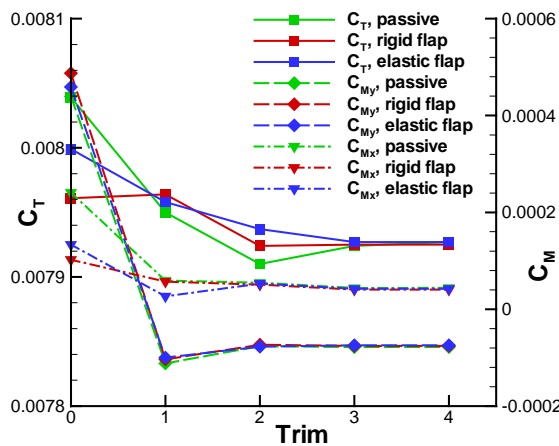


Figure 6: Mean values of rotor load coefficients versus trim iteration

Rotor Performance

The influence of the 2/rev flap control on the rotor performance is depicted in Figure 7 and Figure 8. Figure 7 shows the relative power consumption of the active rotor compared to the passive one, as predicted by the initial HOST trim. The power consumption of the passive rotor has been chosen as reference power. The relative power consumption is plotted on the radial axis, whilst the azimuthal increment of

the flap phase is given on the circumferential axis. Note, that we used the modified polar curves of the rigid flap for the trim computations of both the rigid flap and the elastic trailing edge rotors. Hence, HOST models the rigid flap rotor in its 0th trim, and during the convergence of the weak coupling scheme the CFD solution either introduces the loads of the rigid flap rotor or the elastic trailing edge rotor. From Figure 7 it can be identified, that HOST predicts a small power increase of about 1% of the active flap rotor compared to the passive rotor at an optimum phase angle of $\varphi = 150^\circ$.

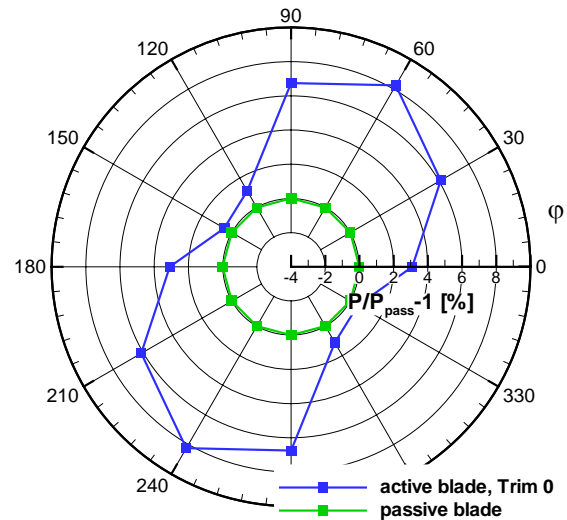


Figure 7: Rotor power over phase angle, trim 0

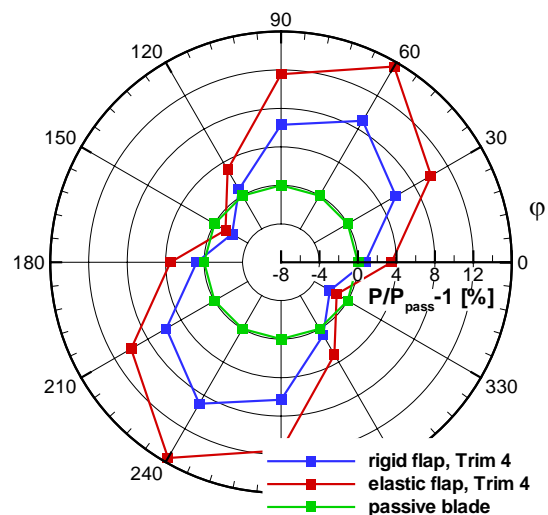


Figure 8: Rotor power over phase angle, trim 4

Figure 8 shows the situation in trimmed state using an equivalent representation. Hence, the reference power is now the power consumption of the passive rotor in trimmed state. As the HOST-internal aerodynamic loads have either been replaced by the CFD loads of the rigid flap rotor or the CFD loads of the elastic trailing edge rotor, we obtain a different relative power

consumption for both rotors in trimmed state. The red line shows the relative power requirement of the elastic trailing edge rotor and the blue line gives the relative power consumption of the rigid flap rotor.

It can be clearly seen that the power requirement of both the rigid flap rotor and the elastic trailing edge rotor falls below the power requirement of the passive rotor at an optimum phase angle of $\varphi = 150^\circ$. The power reduction is approximately 2.5% for the rigid flap rotor and about 1.5% for the elastic trailing edge rotor. Although the phase angle of the relative power minimum matches to the prediction of the initial HOST trim, the prediction in relative power differs by more than 3%. The CFD solution substantiates that it should in fact be possible to achieve a power reduction. In the following we will thus perform a deeper analysis of the effect of active control for the flap phase angle of $\varphi = 150^\circ$.

Figure 9 presents the radial distributions of the sectional pitching moment $C_m Ma^2$ and the sectional normal force $C_n Ma^2$ for both the rigid flap rotor and the elastic trailing edge rotor in comparison to the passive rotor. The distributions are given at $\psi = 150^\circ$, which corresponds to the location of maximum upward flap deflection. Consequently, a positive (nose-up) pitching moment is caused in the flap region. It can be clearly seen, that this effect is even more pronounced for the elastic trailing edge. This is caused by the higher effective deflection angle at the trailing edge (see again Figure 3). Figure 9 shows that the normal force distribution is also significantly influenced by the flap deflection. The upward deflection leads to a nose-up torsion of the blade and consequently to a higher effective angle of attack and a higher normal force. Note, that within the flap region the normal force is locally reduced, as the nose-up torsion of the blade is partially compensated by the reduction of the effective camber of the airfoil.

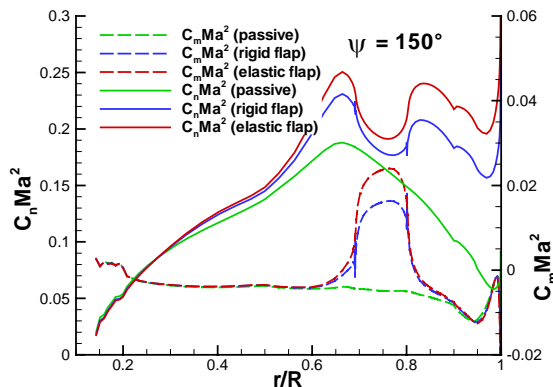


Figure 9: Comparison of radial load distributions

Figure 10 and Figure 11 show azimuthal distributions of the sectional pitching moment $C_m Ma^2$ and the sectional normal force $C_n Ma^2$. Figure 10 shows the distribution within the flap area ($r/R = 0.75$), whereas the radial station of Figure 11 ($r/R = 0.50$) is located inboard of the flap range. As expected, Figure 10 shows that the pitching moment distribution is massively influenced by the deflection of the flap. The strongest effects are observed on the advancing blade side. This statement also holds for the $C_n Ma^2$ -distributions. The most interesting effect of active control can be spotted in Figure 11, looking at the sectional pitching moment distribution inboard of the flap. One can see a pronounced nose-down peak in the distribution of the passive rotor, located around $\psi = 240^\circ$. This peak is significantly reduced by active control. Its amplitude is reduced to approximately 1/3 in case of the rigid flap, and it is even further reduced in case of the elastic trailing edge.

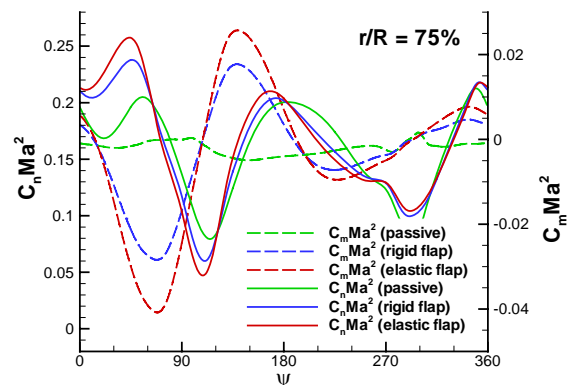


Figure 10: Comparison of azimuthal load distributions ($r/R = 0.75$)

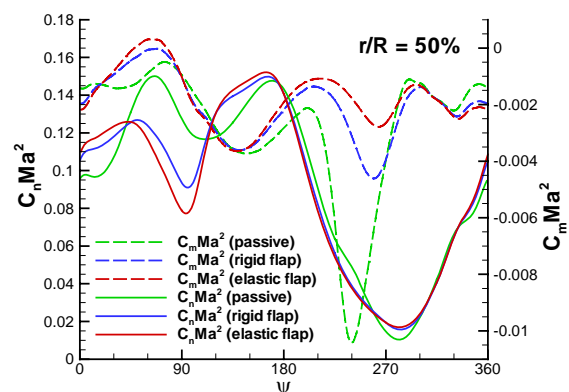


Figure 11: Comparison of azimuthal load distributions ($r/R = 0.50$)

The distinct peak observed for the passive rotor is a typical indication of the Dynamic Stall phenomenon. Figure 11 suggests, that the Dynamic Stall properties can be improved by active control. We will study this finding in more detail with the following Figures.

Figure 12 to Figure 15 show drag distributions on the rotor disk. Note that $C_{Fy}Ma^2$ denotes the force in positive y-direction of the rotating rotor hub system according to HOST convention. Therefore a negative value signifies drag and a positive value a propulsive force in the rotor plane. Figure 12 shows the distribution of the passive rotor and Figure 13 shows the distribution of the active rotor utilizing rigid flaps. The difference in $C_{Fy}Ma^2$ between active rotor (rigid flaps) and passive rotor is given in Figure 14. A negative value denotes higher drag of the active rotor compared to the passive one. Finally, Figure 15 shows the difference in $C_{Fy}Ma^2$ between the two flap configurations, i.e. elastic trailing edge flap minus rigid flap. Consequently, a negative value denotes higher drag of the elastic trailing edge rotor compared to the rigid flap rotor.

Figure 14 shows that compared to the passive rotor active control leads to both regions of increased drag and regions of reduced drag. Regions of reduced drag are mainly located on the retreating blade side. The distinct region of high drag reduction around $240^\circ < \psi < 270^\circ$ and $0.4 < r/R < 0.6$ is related to improvement of the Dynamic Stall situation. Figure 15 reveals that a further drag reduction on the retreating blade side is achieved by the increased control authority of the elastic trailing edge flap. But this further reduction is compensated by the regions of higher drag around $\psi = 30^\circ$ and $\psi = 150^\circ$. Finally, this results in the slightly higher overall power consumption of the elastic flap rotor compared to the rigid flap rotor. However, one should not draw the wrong conclusion that the rigid flap is superior to the elastic flap. The poorer performance of the elastic flap is only due to the increased control authority, caused by the higher effective deflection of the flow.

Figure 16 shows the skin friction contour and streamlines at $\psi = 270^\circ$ for the passive rotor (top), the rigid flap rotor (center) and the elastic flap rotor (bottom). The top Figure clearly shows a complex, highly three-dimensional separation topology for the passive rotor in the region between $r/R = 0.3$ and $r/R = 0.7$. The center and bottom Figures show that the stall region can be significantly reduced by active control. This effect is mainly caused by the nose-down twist deflection of the blade in this azimuth range, which reduces the local geometrical incidence angle of the airfoil and thus the strength of the flow separation.

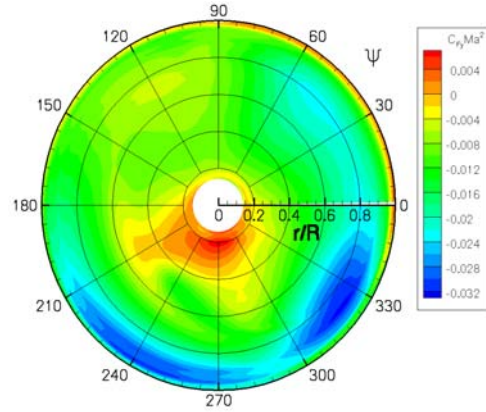


Figure 12: $C_{Fy}Ma^2$ -distribution, passive rotor

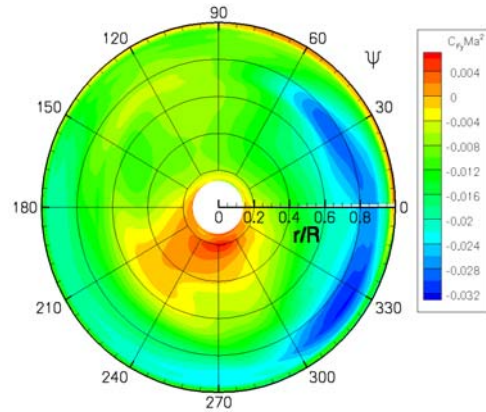


Figure 13: $C_{Fy}Ma^2$ -distribution, rigid flap rotor

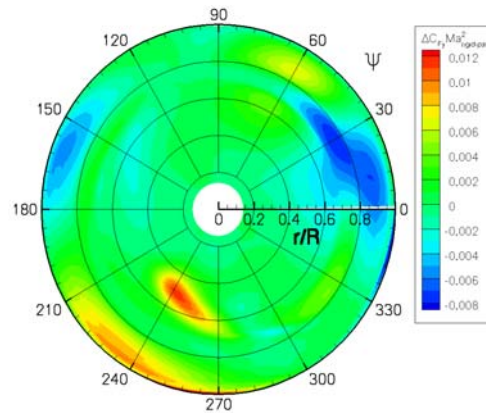


Figure 14: $\Delta C_{Fy}Ma^2$ -distribution, rigid flap rotor minus passive rotor

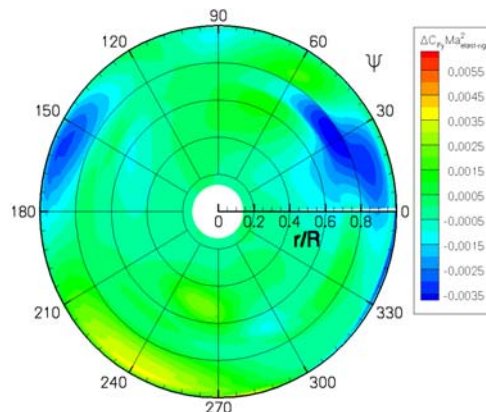


Figure 15: $\Delta C_{Fy}Ma^2$ -distribution, elastic trailing edge rotor minus rigid flap rotor

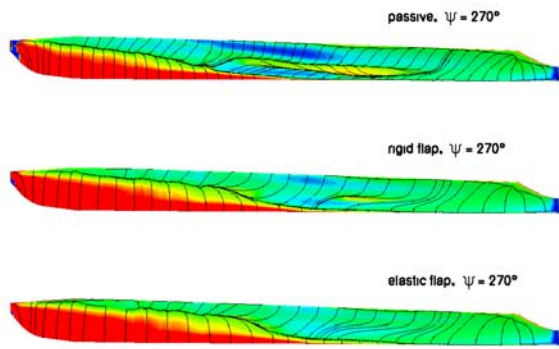


Figure 16: Comparison of passive blades and active blades at $\psi=270^\circ$

Figure 17 substantiates this finding. The Figure shows the elastic blade tip torsion versus azimuth. One can identify an increase of nose-down torsion of approximately 1° around $\psi=250^\circ$ for the rigid flap rotor. An even higher nose-down torsion is observed for the elastic flap rotor which is in line with the findings from Figure 15.

The timewise evolution of the flow separation effect is illustrated by Figure 18 which shows spanwise vorticity contours for radial cuts at $r/R=0.5$, from $\psi=264^\circ$ to $\psi=294^\circ$. The passive rotor is shown in the left column while the rigid flap rotor is given on the right column. One can clearly see that the vortex strength is significantly reduced by active control.

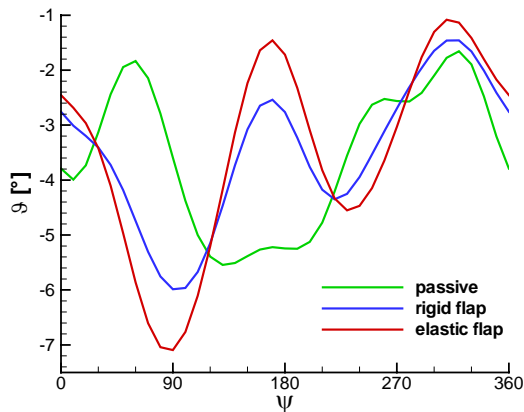


Figure 17: Comparison of elastic blade tip torsion

Flight Speed Sweep for optimum phase angle

The results from the previous section have shown that the minimum power consumption is obtained at a flap phase angle of $\varphi=150^\circ$. Furthermore, it has been shown that the effect of the reduction of required rotor power is related to the positive influence of active control

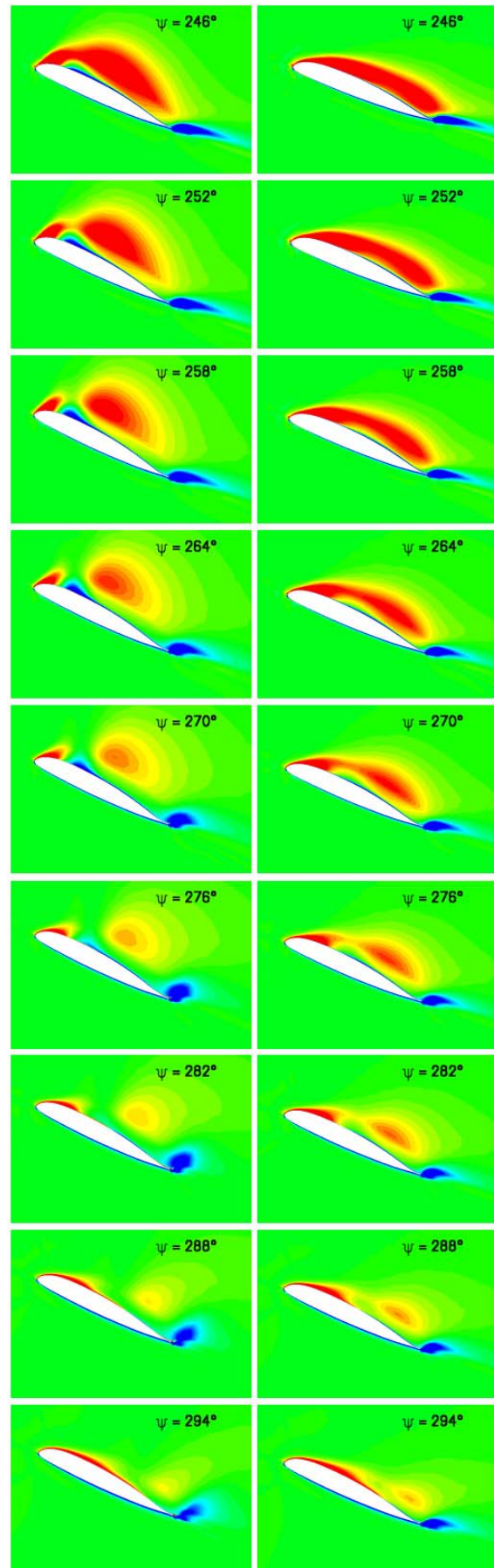


Figure 18: Timewise evolution of spanwise vorticity, $r/R = 0.5$ (left: passive, right: rigid flap)

on the flow separation on the retreating blade side. Hence, it can be expected that the potential of active control with respect to power reduction increases with the increase of non-linear flow effects, i.e. with increasing flight speed and rotor loading. Therefore the influence of a flight speed variation on the rotor performance has been investigated. The phase angle of the control law has been held fixed at the optimum value of $\varphi=150^\circ$. A preliminary investigation^[17] has shown that the optimum phase angle is not sensitive to the flight speed. A phase sweep at 160kts flight speed revealed the same optimum phase angle of $\varphi=150^\circ$.

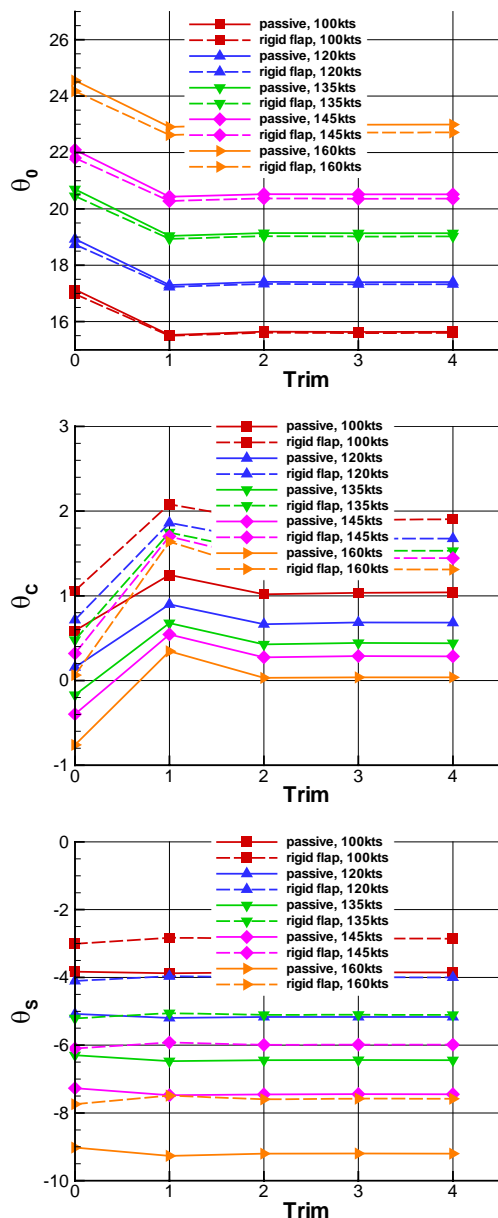


Figure 19: Convergence of collective and cyclic pitch angles

The results presented in this section have been obtained for a helicopter with a reduced take-off weight at a lower flight level. Hence the rotor

loading is reduced compared to the trim condition used for the investigations of the previous section. Nevertheless, it can be assumed that the results with respect to the flight speed variation remain valid and the tendency can be directly transferred towards a higher rotor loading.

Figure 19 shows the trim convergence of the control angles for the investigated flight speeds of 100kts, 120kts, 135kts, 145kts and 160kts. It can be seen that again very good convergence properties have been obtained, even for the highest flight speed at 160kts.

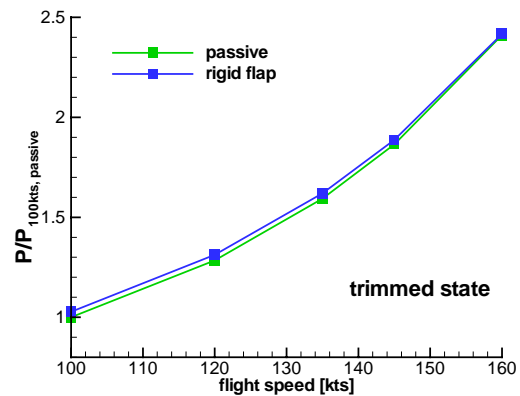


Figure 20: Relative power consumption, reference power: passive rotor at 100kts

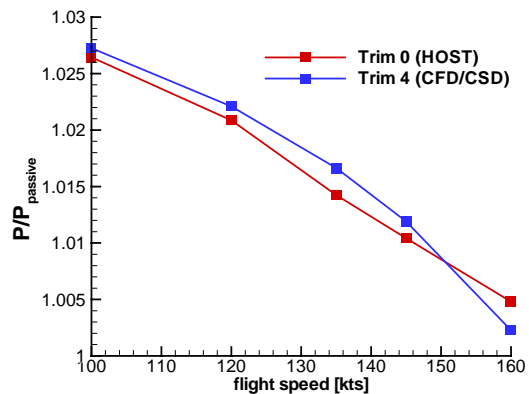


Figure 21: Relative power consumption, reference power: passive rotor at same speed

The performance results are given in Figure 20 and Figure 21. In Figure 20, the power consumption of the passive rotor at 100kts has been used as reference power. The Figure shows that the power requirement of the active rotor exceeds the power requirement of the passive rotor for all flight speeds. However, the relative power increase reduces with increasing flight speed. The same result, in an alternative representation, can be extracted from Figure 21. Here, the relative power consumption of the active rotor compared to the passive one at the same flight speed is plotted versus the flight speed. Both the result of the 0th HOST trim (no

CFD) and the coupled CFD/CSD solution is shown. Again, the relative increase in power consumption decreases with the flight speed. Note, that the coupled CFD/CSD solution predicts a higher power increase than the stand-alone HOST solution for all flight speeds from 100kts to 145kts. At 160kts things look different: Here, the coupled solution predicts a lower power increase which exceeds the power consumption of the passive rotor by only 0.2%.

Thus, we can conclude as follows:

- The potential of active control increases with increasing flight speed, as non-linear flow effects become more dominant.
- The CFD solution is likely to improve the prediction of such non-linear effects

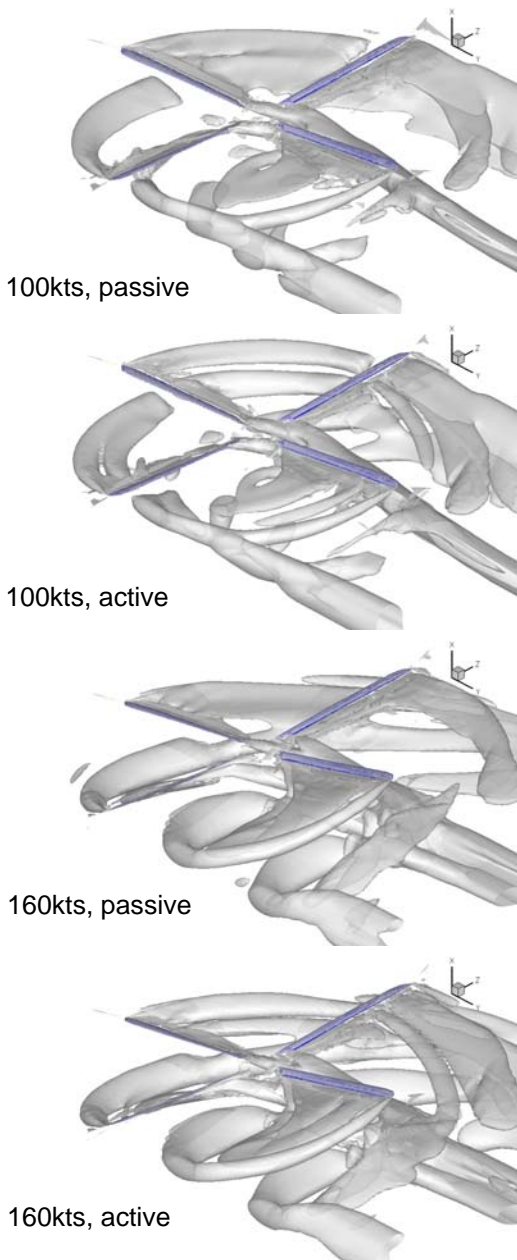


Figure 22: Visualization of 3D flow field

Figure 22 shows exemplarily the 3D flow field obtained for the passive and active rotor at 100kts and 160kts flight speed. The vortex system has been visualized using the λ_2 -criterion of Jeong and Hussain^[18]. The pictures emphasize the high complexity of the resulting flow fields and substantiate the need to introduce nonlinear aerodynamic modeling into the coupled aerodynamic/dynamic rotor solution.

Phase Sweep for FRIENDCOPTER configuration

In this section we present first results that have been obtained for the flap configuration used in the FRIENDCOPTER project. In contrast to the LARS project the discrete trailing edge flap is replaced by a continuous deflection of an elastic trailing edge. The active rotor blade features one elastic trailing edge segment with a chordwise extent of 20% chord and the radial position $r/R = 0.56 - 0.91$. Hence, the radial extension of the actuated blade part is approximately three times larger than in case of the LARS configuration. At the radial borders the deflection of the trailing edge is continuously reduced towards zero within a smoothing range of 0.2m. A trailing edge amplitude of 1.5mm has been used for the investigation. Both flap control law and flight condition have been adopted from the flight case presented in the first results section. Note, that the HOST dynamic blade model was modified in order to match the actual FRIENDCOPTER blade properties.

In contrast to our previous investigations we were able to significantly improve the quality of the blade grid structures by the usage of a multi-block topology in conjunction with the multi-block grid deformation tool. The topology of the grid has already been presented in Figure 2. The grid uses a C-topology in chordwise direction and an O-topology in spanwise direction. It consists of 22 blocks and 1,003,008 cells in total.

The trim convergence of the control angles is given in Figure 23. It can be seen that the convergence properties have deteriorated compared to our previous investigations using the LARS flap geometry. This is likely to be caused by the larger spanwise extension of the flap, leading to an increased control authority. Figure 23 shows that convergence is poorest for the flap phase angles of $\varphi=30^\circ$ to $\varphi=90^\circ$. As we will show further below these phase angles lead to the maximum power increase compared to the passive rotor. Hence, the poor con-

vergence behaviour is likely to be caused by an unstable dynamic excitation of the blade. Good convergence has been achieved for the passive rotor and the remaining flap phase angles. This is confirmed by Figure 24 which proves that the passive rotor and the active rotor at $\varphi=150^\circ$ have actually been trimmed towards the same state with an acceptable accuracy.

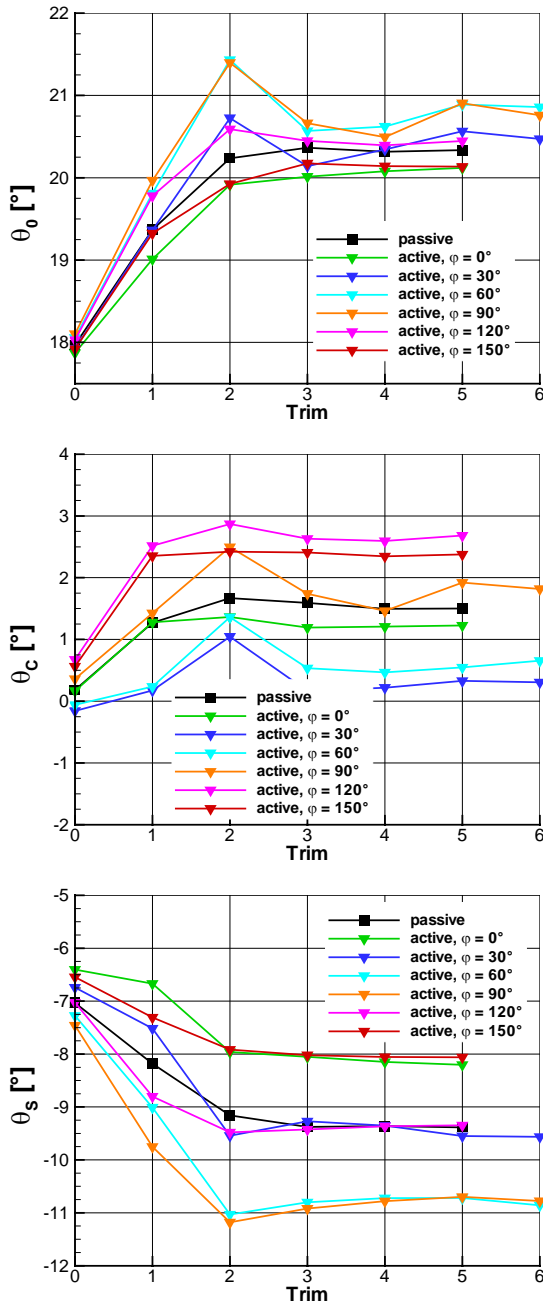


Figure 23: Convergence of collective and cyclic pitch angles

Figure 25 and Figure 26 show comparisons between the 2D HOST loads and the CFD loads, both given in trimmed state for the active rotor at $\varphi=150^\circ$ phase angle. Figure 25 shows the radial distribution of thrust and pitching moment at $\psi=60^\circ$ (maximum downward flap

deflection), whereas the azimuthal distribution at $r/R = 0.75$ (within the flap area) is compared in Figure 26. The Figures show that the 2D and 3D load prediction generally match quite well. As expected the CFD loads show a smoother distribution of the loading in the smoothing range of the spanwise flap boundaries.

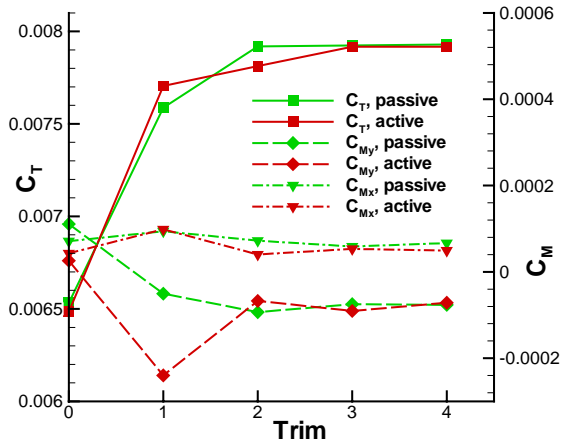


Figure 24: Mean values of rotor load coefficients versus trim iteration

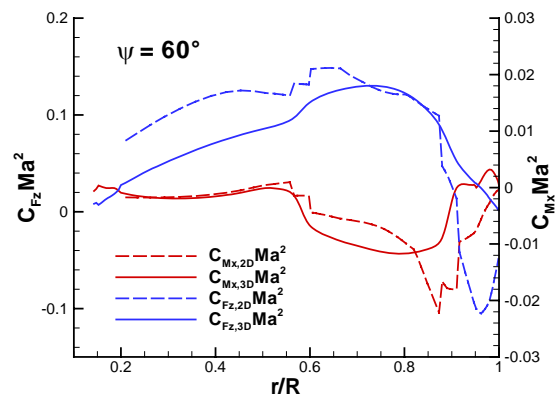


Figure 25: Comparison between HOST loads and CFD loads in trimmed state, $\psi=60^\circ$

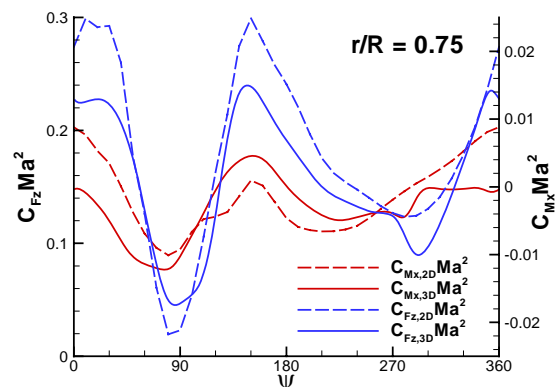


Figure 26: Comparison between HOST loads and CFD loads in trimmed state, $r/R = 0.75$

Finally, Figure 27 shows the relative power consumption of the active rotor compared to the passive one, both for the 0th HOST trim and in trimmed state. One can see, that both HOST

and the coupled solution predict a roughly 1.5% power increase in the optimum phase angle. The initial HOST trim predicts an optimum phase angle of $\varphi=90^\circ$, which constitutes a conspicuous deviation from the previous findings for the LARS flap configuration. The CFD solution corrects the optimum phase angle to the value of $\varphi=150^\circ$, which coincides with the one obtained for the LARS flap geometry.

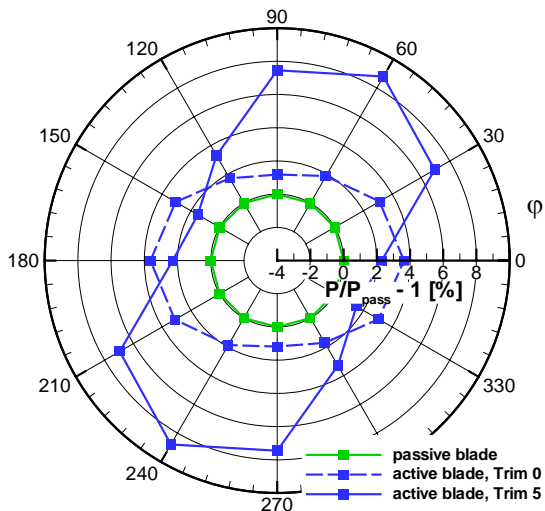


Figure 27: Rotor power over phase angle

Conclusions & Perspectives

We presented rotor performance results for different concepts of actively controlled servo flap rotors. The weak coupling method between CFD and a flight mechanics code was applied in order to trim the rotor and allow for a meaningful comparison between the active and passive rotor.

The trimmed CFD/CSD results suggest that it is in fact possible to achieve a reduction of the required rotor power using a 2/rev flap control law. The coupled solution suggests a power saving of approximately 2.5% at the optimum flap phase angle. The power reduction is due to a positive effect of active control on the Dynamic Stall region on the retreating blade side.

A flight speed sweep at optimum flap phase angle revealed that the potential of active flap control increases with increasing dominance of non-linear flow effects, i.e. increasing forward flight speed.

Our future work will focus on further investigations on the FRIENDCOPTER active rotor concept. Up to now we were only able to present first preliminary results. Further activities will also be focussed on questions that arose during this study:

- Investigation of the influence of different turbulence models on the performance result
- Investigation of the influence of different flap control laws with respect to performance
- Introduction of a relaxation technique in the weak coupling load exchange procedure in order to improve the trim convergence for "critical" cases
- Comparison of the results to flight test data.

Acknowledgments

The authors would like to thank the German Ministry of Economy and Technology (BMWi) for its funding in the framework of CHANCEII (grant 20H0303A) and LARS (grant 20H0304A).

References

- [1] Kloeppel, V., Enenkl, B., and Strehlow, H.: "Rotor Blade Control by Active Helicopter Servo Flaps", International Forum on Aeroelasticity and Structural Dynamics 2005, Munich, Germany, June 2005.
- [2] Enenkl, B., Klöppel, V., Preißler, D., and Jänker, P.: „Full Scale Rotor with Piezoelectric Actuated Blade Flaps“, Paper 89, 28th European Rotorcraft Forum, Bristol, UK, September 2002.
- [3] Dieterich, O., Enenkl, B., and Roth, D.: "Trailing edge flaps for active rotor control, aeroelastic characteristics of the ADASYS rotor system", Alfred P. Gessow Award for Best Paper at American Helicopter Society 62nd Annual Forum, Phoenix, AZ, May 2006.
- [4] Roth, D., Enenkl, B., and Dieterich, O.: "Active rotor control by flaps for vibration reduction – full scale demonstrator and first flight test result", Proceedings of the 32nd European Rotorcraft Forum, Maastricht, The Netherlands, September 2006.
- [5] Friedmann, P., Liu, L., Kim, I., and Bernstein, D.: "Rotor performance enhancement and vibration reduction in presence of dynamic stall using actively controlled flaps", Proceedings of the 32nd European Rotorcraft Forum, Maastricht, The Netherlands, September 2006.
- [6] Cheng, R., Theodore, C.R., and Celi, R.: "Effects of Two/rev Higher Harmonic Control on Rotor Performance", Journal of the American Helicopter Society, Vol. 48, No. 1, pp. 18-27, January 2003.
- [7] Benoit, B., Dequin, A.-M., Kampa, K., Grünhagen, W. v., Basset, P.-M., and Gimonet, B.: "HOST: A General Helicopter

- Simulation Tool for Germany and France*”, American Helicopter Society, 56th Annual Forum, Virginia Beach, Virginia, May 2000.
- [8] Kroll, N., Einfeld, B. and Bleecke, H.M.: “*The Navier-Stokes Code FLOWer*”, Volume 71 of Notes on Numerical Fluid Mechanics, pages 58-71. Vieweg, Braunschweig, 1999.
- [9] Jameson, A., Schmidt, W. and Turkel, E.: “*Numerical Solutions of the Euler Equations by Finite Volume Methods Using Runge-Kutta Time-Stepping Schemes*”, AIAA-Paper 81-1259, 1981.
- [10] Jameson, A.: “*Time Dependent Calculation Using Multigrid, With Applications to Unsteady Flows Past Airfoils and Wings*”, AIAA-Paper 91-1596, 1991.
- [11] Altmikus, A. Wagner, S., Beaumier, P., and Servera, G.: “*A Comparison: Weak versus Strong Modular Coupling for Trimmed Aeroelastic Rotor Simulations*”, American Helicopter Society 58th Annual Forum, June 2002.
- [12] Servera, G., Beaumier, P., and Costes, M.: “*A weak coupling method between the dynamics code HOST and the 3D unsteady Euler code WAVES*”, 26th European Rotorcraft Forum, The Hague (The Netherlands), Sept. 2000.
- [13] Pahlke, K., and Van der Wall, B.: “*Calculation of Multibladed Rotors in High-Speed Forward Flight with weak Fluid-Structure-Coupling*”, 27th European Rotorcraft Forum, Moscow, Russia, September 2001.
- [14] Dietz, M., Krämer, E., Wagner, S., and Altmikus, A.: “*Weak Coupling for Active Advanced Rotors*”, 31st European Rotorcraft Forum, Florence, Italy, September 2005.
- [15] Hierholz, K.-H.: “*Ein numerisches Verfahren zur Simulation der Strömungs-Struktur-Interaktion am Hubschrauberrotor*”, Dissertation, Institut für Aerodynamik und Gasdynamik, Universität Stuttgart, Fortschritt-Berichte VDI Reihe 7, Nr. 375, VDI-Verlag, Düsseldorf, 1999.
- [16] Altmikus, A., and Knutzen, B.: “*Trimmed Forward Flight Simulation with CFD featuring Elastic Rotor Blades with and without Active Control*”, American Helicopter Society 63rd Annual Forum, Virginia Beach, VA, May 2007.
- [17] Höfler, Florian: “*Aeroelastische Untersuchungen an aktiven Rotoren mit einem automatisierten Kopplungs- und Trimmverfahren*”, Diplomarbeit, Institut für Aerodynamik und Gasdynamik, Universität Stuttgart, 2006.
- [18] Jeong, J., Hussain, F., “*On the Identification of a Vortex*”, Journal of Fluid Mechanics, Vol. 285, pp. 69-94, 1995.